Experimental Study on Debonding Detection for Grouted Jacket Connection of an Off-Shore Wind Turbine Supporting Structure Specimen with PZT Patches

---

QIAN LIU[1], BIN XU[*,1,2], XINHAI ZHU[1], JIANG WANG[1]
and WEI HU[3]

ABSTRACT

Grouted jacket connections (GJCs) have been widely used to connect longitudinal components of offshore wind turbine supporting structures. Debonding defects detection in GJCs is critical for the safety and serviceability of offshore wind turbine support structures. In this paper, an interface debonding detection approach for a scaled GJC specimen using both surface stress wave and Electromechanical impedance (EMI) measurement is proposed with Piezoelectric lead zirconate titanate (PZT) patches. The scaled GJC specimen with various mimicked interface debonding detects is designed. Based on the surface stress wave measurements of PZT sensors arranged with a one pitch and multiple catch (OPMC) configuration, the regions of the mimicked defects are estimated using the intersections of the surface stress wave propagation paths with abnormal measurements. EMI measurements of PZT sensors located in the estimated debonding regions are used to accurately identify the dimension of the mimicked debonding defects using the root mean square deviation (RMSD) index of the impedance measurements of PZT sensors. The visualized debonding region is close to the actual location of the mimicked debonding defect.

1 INTRODUCTION

The operation, repair and maintenance expenditures of the supporting structures of offshore wind turbines account for the life-cycle cost (LCC) of offshore wind farms. Therefore, ensuring the safety and reliability of wind turbine supporting structures under harsh marine environment is particularly important. Condition monitoring and nondestructive defect detection for offshore wind turbine supporting structures subjected to dynamic loads such as strong wind, earthquake and wave loads attracted great attentions in civil engineering fields [1].

---

[1] College of Civil Engineering, Huaqiao University, Jimei Avenue 668, Xiamen, Fujian, 361021, China
[2] Key Laboratory for Intelligent Infrastructure and Monitoring of Fujian Province (Huaqiao University), Jimei Avenue 668, Xiamen, Fujian, 361021, China
[3] CCCC Second Harbor Engineering Company LTD, Xi Dong Hu Avenue 11, Wuhan, Hubei, 430040, China
*Correspondence: binxu@hqu.edu.cn

Monitoring technologies for blade fatigue and bolt connection of onshore and offshore wind turbines have been developed [2, 3]. The grouted jacket connections (GJCs) widely used to connect steel tubes of the platform and pile foundations under sea water are the critical parts of the supporting structures of offshore wind turbines. The overall safety and reliability of the wind turbine supporting structures are heavily dependent on the quality of the GJCs, where the interface debonding between grouting materials and steel tubes in GJCs might occur due to poor grouting quality control [4]. Developing efficient interface debonding defect detection approaches for GJCs has been desired in practice.

Unfortunately, most traditional nondestructive testing (NDT) inspection methods are inefficient for interface bonding condition monitoring of GJCs. In recent decades, damage detection techniques using Piezoelectric lead zirconate titanate (PZT) patches have shown their efficiency in detecting interface defects in civil engineering structures. Ma et al. [5] proposed an active crack detection technique for Carbon Fiber Reinforced Polymer (CFRP) under static load using Lamb wave measurements with PZT patches. For existing concrete-filled steel tube (CFST) members as typical steel-concrete composite structures, Xu et al. [6] established a multi-physics field finite element model to compare the stress wave fields in the cross sections of CFST components without and with debonding defects. Considering the convenience of the installation of PZT actuators and sensors and stress wave measurement, Xu et al. [7] proposed an interface debonding defect detection approach for CFST members with surface stress wave measurement propagating along steel tube of the specimens. Even electromagnetic methods were efficient for debonding detection of concrete members strengthened with CFRP materials, due to the shielding effect of steel tube located at the outside surface of GJCs, electromagnetic methods do not work for the detection of interface debonding defects of GJCs. Electromechanical impedance (EMI) measurement with PZT patches is highly sensitive to local minor damages or defects in concrete structures, reinforced concrete (RC) structures and aerospace structures but unsusceptible to external environmental and boundary conditions [8,9]. The feasibility of monitoring approach for minor looseness of flange bolts under noisy environment using EMI measurement was verified in harsh offshore environments [10].

In this study, surface stress wave measurements with a one pitch and multiple catch (OPMC) configuration are firstly used to preliminarily determine the location of mimicked interface debonding defects of a scaled GJC specimen. The range of the mimicked interface debonding defects are detected successfully and visualized with the help of EMI technology.

2 PRINCIPLE OF INTERFACE DEBONDING DEFECT DETECTION WITH SURFACE STRESS WAVE AND EMI MEASUREMENTS

2.1 Surface Wave Measurement with OPMC Configuration for Interface Debonding Region Preliminary Estimation

The principle for interface debonding detection for a GJC specimen with surface stress wave measurement where PZT patches are used as actuators and sensors is shown in Figure 1. The stress waves pass along the steel tube and enter the internal grouting material.

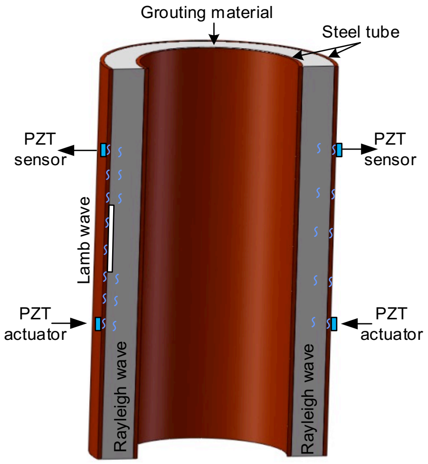

Figure 1. Debonding detection with surface wave measurements.

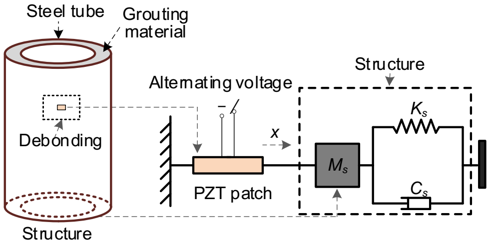

Figure 2. EMI technology for debonding detection.

When the stress waves arrive at the starting point of the interface debonding defect, its propagation from the steel tube to the grouting material is blocked and the Rayleigh waves transfer to Lamb waves in the steel tube with debonding accordingly. The surface stress wave measurement of the PZT sensor outside of the end point of the debonding defect should be greater than that of the PZT sensor located at the steel tube without debonding [7,11]. By comparing the surface stress wave measurement, the debonding defect within the wave travelling path can be detected.

2.2 EMI Measurement and Evaluation Index

The principle of interface debonding defect detection for a GJC specimen using EMI measurement with surface-mounted PZT patches is shown in Figure 2. The PZT patch can be simplified as a single-degree-of-freedom system considering only the axial compression deformation and coupled with the host structure [12]. The electrical impedance of the PZT sensor is coupled with the mechanical impedance of the host structure. When interface debonding defect occurs between the steel tube and the grouting material of the specimen, the local stiffness at the location of the debonding defect decreases, which results in a change in the mechanical impedance of the structure and the coupling EMI of the PZT sensor. Therefore, the interface debonding can be identified by comparing the changes in EMI collected by PZT sensors at different locations in the host structure.

3 EXPERIMENTAL STUDY

3.1 Design of a Scaled GJC Specimen and Test Setup

A scaled GJC specimen with mimicked interface debonding defects is designed in lab. As shown in Figure 3, the GJC specimen has a height of 1200mm and the thickness of the steel tube is 10mm. The diameters of the inner and outer steel tube are 500mm and 600mm, respectively. Acrylic material is used to mimic two interface debonding defects with a dimension of 100mm×50mm and 100mm×150mm, respectively. The mimicked debonding defects have a thickness of 5mm.

Figure 3. Sample diagram.

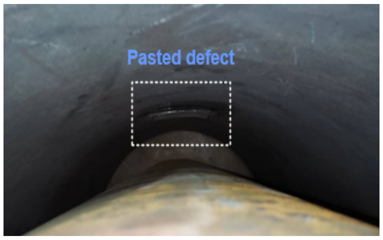

Figure 4. Artificially mimicked debonding defects.

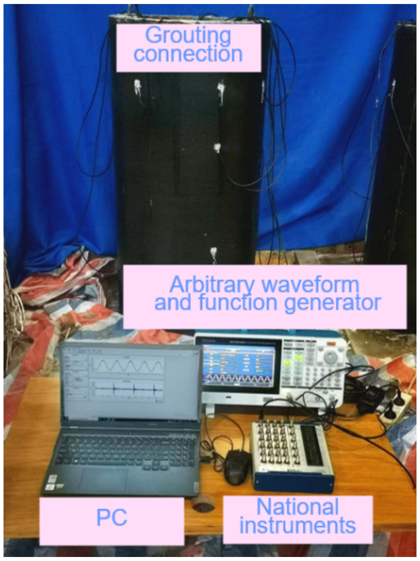

Figure 5. Detection system with surface wave measurement.

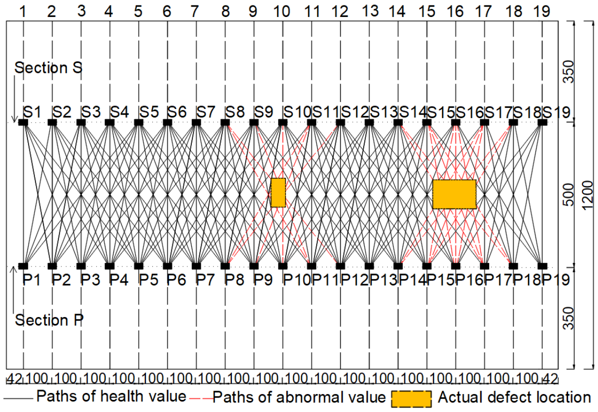

Figure 6. Position and numbering of the PZT.

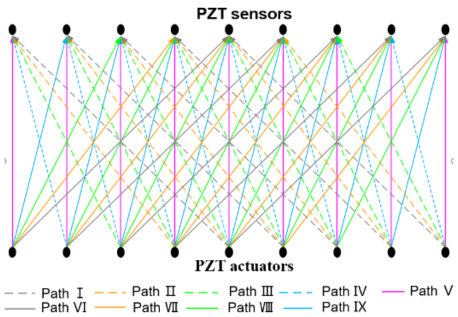

Figure 7. OPMC measurement configuration and paths definition.

The installation of the mimicked interface debonding defect is shown in Figure 4. The test setup is shown in Figure 5. PZT patches with an identical size of 15 mm×10 mm×0.5 mm are used as both actuators and sensors, the material properties and the installation procedure of the PZT patches can be found in the previous study [7]. The position and PZT patches in the stretch-out view of the outer tube as shown in Figure 6. A total of 19 PZT patches are used in each cross section. When one PZT actuator at section P is excited, nine PZT sensors at section S are employed to measure the surface wave. Paths with the same measurement distance and measurement angle are grouped and shown with an identical color as shown in Figure 7. A continuous sinusoidal signal with an amplitude of 10 V and a frequency of 50 kHz is used for excitation.

3.2 Preliminary Interface Debonding Detection with Surface Wave Measurement

The amplitudes of the stress wave measurements in each group are arranged in order from the smallest to the largest, that is, $X_1 \leq X_2 \leq \ldots \leq X_n \leq X_{n+1}$. The significantly larger data than the adjacent one in line are judged as a suspicious data. Then the smallest one of these suspicious data (assumed X_n) together with its preceding data are used to calculate the mean value m_x and standard deviation s_x by Eqs. (1) and (2). The judgment value X_0 of the abnormal situation is calculated according to Eq. (3).

$$m_x = \Sigma X_i / n \tag{1}$$

$$s_x = \sqrt{(\Sigma X_i^2 - n \cdot m_x^2)/(n-1)} \tag{2}$$

$$X_0 = m_x + \lambda_1 \cdot s_x \tag{3}$$

where λ_1 is obtained by the specification [13], X_i is the i-th measurement value, and n is the number of data involved in the statistics.

Compare the judgment value X_0 with the minimum value X_n of the suspicious data, When $X_0 \leq X_n$, then X_n and the data arranged after it are abnormal values, and X_n will be removed. $X_1 \sim X_{n-1}$ will be used to calculate and discriminate until no abnormal value is identified. When $X_0 > X_n$, X_{n+1} should be put in to calculate and discriminate again.

Table I shows the amplitudes of PZT sensor measurements corresponding each path. Based on abnormal value judgement approach described above, the abnormal values in each group are identified and shown in bold in Table I. The wave traveling path corresponding the identified abnormal values are shown in red in Figure 6, where the two regions enclosed by the abnormal paths are the preliminarily detected defect location. Results show that two detected regions match well with the actual location of the artificially mimicked debonding defects.

TABLE I. SURFACE WAVE MEASUREMENT AMPLITUDES AND THE ABNORMAL VALUES

Actuator number	**Groups and corresponding path of surface wave measurements**								
	Group 1		**Group 2**		**Group 3**		**Group 4**		**Group 5**
	I	**VI**	**II**	**VII**	**III**	**VIII**	**IV**	**IX**	**V**
1	2.42	2.37	3.09	2.72	3.14	2.87	3.35	3.34	3.54
2	2.33	2.44	2.77	2.60	2.82	2.44	2.94	3.21	3.27
3	2.75	2.62	2.85	3.24	2.94	2.72	3.58	2.82	3.64
4	1.97	2.52	3.12	3.23	2.65	2.53	3.49	3.53	3.36
5	2.39	2.67	2.61	2.95	3.23	2.80	2.66	3.33	3.42
6	2.54	2.85	2.67	2.57	2.59	2.97	2.81	3.46	3.51
7	2.62	2.89	3.15	2.68	2.97	2.62	3.27	3.29	3.09
8	2.87	**4.54**	2.76	**4.43**	3.77	3.03	3.32	3.51	3.84
9	2.32	2.53	3.26	3.21	3.52	**5.17**	2.76	3.24	3.43
10	2.64	2.75	3.21	2.70	2.98	2.64	3.54	3.55	**6.50**
11	2.24	2.47	**4.32**	2.84	**5.15**	3.08	2.95	2.87	4.05
12	**4.23**	2.60	2.94	2.65	3.26	3.37	3.61	3.59	3.53
13	2.38	2.44	2.85	2.77	3.14	3.16	2.73	3.82	2.93
14	2.52	**4.16**	3.37	**4.66**	2.72	3.22	3.88	4.35	4.12
15	2.95	2.33	3.13	**4.52**	3.23	**5.60**	2.94	**6.36**	3.77
16	2.43	2.44	2.42	2.64	2.81	2.93	**5.82**	**5.73**	**6.96**
17	2.78	2.91	**4.27**	3.17	**4.96**	2.73	**5.34**	3.44	3.44
18	**3.97**	2.65	**4.64**	3.32	3.37	2.65	3.47	3.67	3.24
19	2.51	3.27	3.15	2.92	3.45	3.17	3.36	3.72	4.11
Judgment value X_0	3.29		3.64		3.92		4.37		4.95

3.3 Detailed Interface Debonding Localization Detection with EMI

Based on the preliminary defect region detection result using surface stress wave measurement described above, more PZT patches are arranged in the preliminary regions for the purpose of detecting debonding more correctly using the EMI technology. To further quantify the changes in the impedance signal of the PZT sensors, the root mean square deviation (RMSD) damage index is defined as follows.

$$RMSD_i = \sqrt{\frac{\sum_{j=1}^{N} (Z_{i,j}^{1} - Z_{i,j}^{0})^2}{\sum_{j=1}^{N} (Z_{i,j}^{0})^2}} \times 100\% \tag{4}$$

where $Z_{i,j}^{1}$ represents the impedance test data of the *i*-th PZT sensor at the *j*-th frequency, *N* is the total number of frequency points, and $Z_{i,j}^{0}$ is the average of the impedance of PZT sensors at healthy locations at the *j*-th frequency.

Figure 8 shows the PZT sensors arrangement spaced 100mm apart vertically and 50mm apart horizontally in the preliminarily detected defect regions. The vertical PZT sensors are numbered as A1-A6 and the horizontal PZT sensors are numbered as B1-B5. For comparison, PZT sensors labelled as A1-H~A6-H are mounted at a healthy location of the specimen with identical boundary conditions as that of A1~A6. The EMI of each PZT sensor is measured at frequency range from 100 kHz to 700 kHz with a frequency interval of 0.375 kHz. The EMI measurement system is shown in Figure 9.

Figures 10-11 show the impedance curves of the PZT sensors at different locations. Figure 10 shows that the impedance curves of PZT sensors (A1, A2) located at the preliminary defect region match well with the average impedance curves of the three PZT sensors (A1-H, A2-H, A3-H) at healthy locations, indicating that there is no interface debonding defect at this location. However, the impedance curve of the PZT sensor (A3) located at the boundary of the preliminary defect region has obvious fluctuations and new peak occurs, which indicates the debonding defect at this location leads to a change in local stiffness and results in a new local frequency. Figure 11 shows that the impedance curve of the PZT sensor (B1) is similar to the that of PZT sensors at healthy location, which indicates there are no debonding defects in this location. However, the impedance curves of the PZT sensors (B2, B3) located at the preliminary defect region leads to significant fluctuations and new peaks, which confirms the existence of debonding defects. Similar results can be found for EMI measurements of symmetrically located PZT sensors. It suggests that the defect location can be detected successfully using EMI measurements.

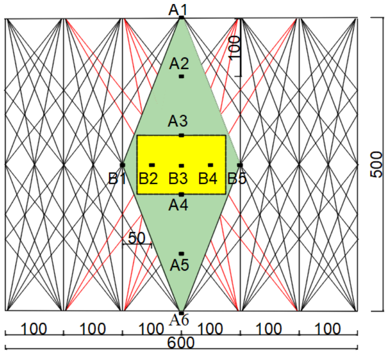

Figure 8. PZT sensor layout (unit: mm).

Figure 9. EMI measurement and detection system.

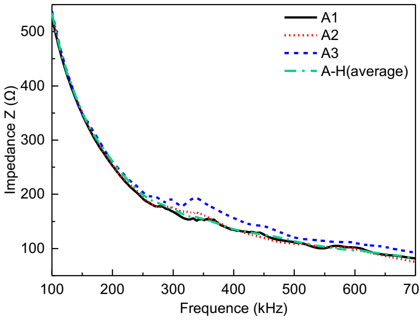

Figure 10. Impedance of PZT sensors at point A1-A3.

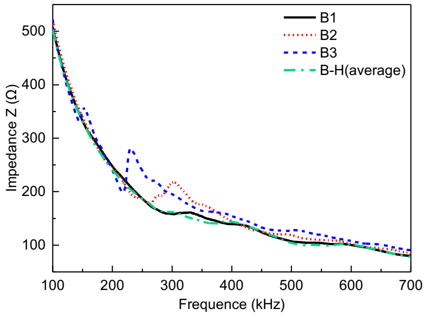

Figure 11. Impedance of PZT sensors at point B1-B3.

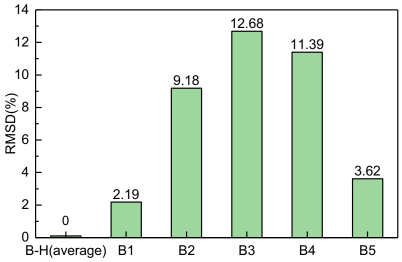

Figure 12. RMSD values of impedance curves at point A1-A6.

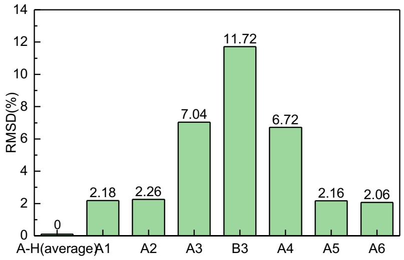

Figure 13. RMSD values of impedance curves at point B1-B5.

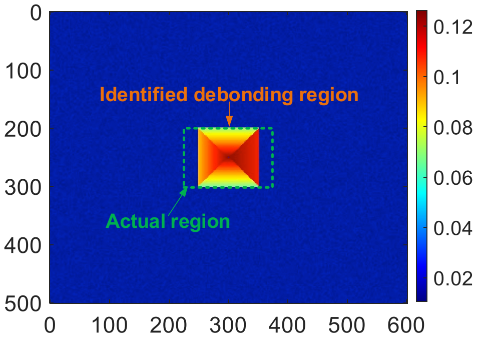

Figure 14. RMSD interpolation mapping results.

Figures 12-13 show the RMSD values of the impedance signals collected from all PZT sensors. It can be seen that the RMSD values at A3, B3, A4, B2, and B4 are significantly greater than them of other measurement points without defect. The RMSD value can distinctly reflect the location of the interface debonding defect, and the existence of the defect significantly increases the damage index. By an interpolation method based on the RMSD values of the five PZT sensors (A3, B3, A4, B2, and B4), the distribution of the RMSD values of the areas covered by the five PZT sensors are determined and mapped to a color matrix using the colormap function. Figure 14 shows the RMSD mapping results that can be treated as a visualization of the identified interface debonding defects. Results show that the identified debonding region is close to the actual region.

5 CONCLUSIONS

In this study, an interface debonding detection and visualization method for GJCs using both surface stress wave and EMI measurements was proposed and experimentally verified with a scaled GJC specimen with artificial mimicked interface debonding defects. Based on the experimental study, the following conclusions can be made:

(1) To quickly and effectively determine the existence of defects and to preliminarily localize the interface debonding defect in GJC specimen, an abnormal path judgement method using surface stress wave measurement is proposed with an OPMC configuration. Test results show that the regions covered by abnormal surface stress wave measurements paths can be treated a preliminary estimation of the mimicked debonding defects are located.

(2) To further determine the interface debonding defect region in detail, EMI measurements of PZT sensors arranged in the preliminarily determined debonding regions were carried out. Results show that EMI measurement curves of PZT sensors within the mimicked debonding region are obviously different from them at the healthy regions.

(3) By an interpolation method based on the RMSD values of PZT sensors at the preliminarily determined debonding region, the detailed debonding region is visualized and the result matches well with the actual artificially mimicked interface debonding defects.

REFERENCES

1. Le, T. C., T. H. T. Luu, H. P. Nguyen, T. H. Nguyen, D. D. Ho, and T. C. Huynh. 2022. “Piezoelectric impedance-based structural health monitoring of wind turbine structures: Current status and future perspectives,” *Energies.*, 15(15): 5459.
2. Nguyen, T. C., T. C. Huynh, J. H. Yi, and J. T. Kim. 2017. “Hybrid bolt-loosening detection in wind turbine tower structures by vibration and impedance responses,” *Wind. Struct*., 24: 385-403.
3. Chen, T., X. Wang, X.L. Gu, Q. Zhao, G. K. Yuan, and J. C. Liu. 2019. “Axial compression tests of grouted connections in jacket and monopile offshore wind turbine structures,” *Eng. Struct.,* 196: 1-19.
4. Li, W., D. Wang, and H. L. Han. 2017. “Behaviour of grout-filled double skin steel tubes under compression and bending: Experiments,” *Thin. Walled. Struct.*, 116: 307-319.
5. Ma, X. S., K. Bian, J. Y. Lu, and K. Xiong. 2016. “Experimental research on detection for interface debond of CFRP T-joints under tensile load,” *Compos. Struct.*, 158: 359-368.
6. Xu, B., H. B. Chen, and S. Xia. 2017. “Wave propagation simulation and its wavelet package analysis for debonding detection of circular CFST members,” *Smart. Struct. Syst.*, 19(2): 181-194.
7. Xu, B., L. L. Luan, H. B. Chen, J. Wang, and W. T. Zheng. 2019. “Experimental study on active interface debonding detection for rectangular concrete-filled steel tubes with surface wave measurement,” *Sensors*, 19: 3248.
8. De Castro, B.A., F. G. Baptista, and F. Ciampa. 2019. “Comparative analysis of signal processing techniques for impedance-based SHM applications in noisy environments,” *Mech. Syst. Signal Pr.*, 126: 326-340.
9. Ai, D. M., H. Luo, and H. P. Zhu. 2019. “Numerical and experimental investigation of flexural performance on pre-stressed concrete structures using electromechanical admittance,” *Mech. Syst. Signal. Pr.*,128: 244-265.
10. Jiang, X., X. Zhang, and Y. X. Zhang. 2020. “Evaluation of Characterization Indexes and Minor Looseness Identification of Flange Bolt Under Noise Influence,” *IEEE Access.*, 8: 157691-157702.
11. Chen, H. B., B. Xu, T. M. Zhou, and Y. L. Mo. 2019. “Debonding detection for rectangular CFST using surface wave measurement: test and multi-physical fields numerical simulation,” *Mech. Syst. Signal. Pr.*, 117(15): 238-254.
12. Liang, S. Z. C., and C. A. Rogers. 1994. “A Dynamic Model of Piezoelectric Actuator-Driven Thin Plat,” *Proceedings of the SPIE, Smart. Struct. Mater.*, 2190:550-562.
13. China Association for Engineering Construction Standardization. “Technical specification for inspection of concrete defects by ultrasonic method,” CECS 21-2000, 13-16.